JOURNAL OF GUIDANCE, CONTROL, AND DYNAMICS
Vol. 43, No. 2, February 2020

Real-Time Estimation of Bare-Airframe Frequency Responses from Closed-Loop Data and Multisine Inputs

Jared A. Grauer*
NASA Langley Research Center, Hampton, Virginia 23681
and
Matthew J. Boucher†
NASA Armstrong Flight Research Center, Edwards, California 93523

DOI: 10.2514/1.G004574

A method is presented for estimating frequency responses of multiple-input multiple-output bare-airframe dynamics from flight test data containing feedback control and/or mixing of control effectors. Orthogonal phase-optimized multisines are used to simultaneously excite each input with unique harmonic frequencies, at which frequency responses are computed as ratios of output-to-input Fourier transform data. The confounding effects of feedback and mixing are resolved by interpolation of the frequency responses. The analysis can be run in batch for postflight analysis, or in real time as the aircraft is flying. The effectiveness of the method was verified using simulations of the subscale T-2 generic transport airplane with rate feedback. The method was also demonstrated using flight test data from the X-56A MUTT aeroelastic airplane, which was flown with both feedback control and mixing.

I. Introduction

A COMMON goal in aircraft system identification is to use measured data to determine a bare-airframe dynamics model that predicts motion arising from control surface deflections. However, it is often necessary to fly the aircraft with a control system active, and/or with mixing of multiple control effectors. Examples include stability augmentation, control allocation using redundant control effectors, and an aileron–rudder interconnect. In these cases, the modeling inputs become correlated and system identification results degrade [1–3].

One solution to this problem is to add unique excitations to each input command, directly at the control effector level, after the control system and mixer. If the correlation coefficients of the inputs are lowered to below about 0.9 in absolute value, parameter estimation methods such as equation error and output error can be applied in the usual manner to successfully identify bare-airframe dynamics from closed-loop data [1,2]. This approach was first applied during testing of the open-loop unstable X-29A airplane and has been successfully used in subsequent flight tests with the F-18 HARV, X-31, F-15B ACTIVE, X-43A Hyper-X, T-2 generic transport, X-56A MUTT, and many others.

If the identification involves matching frequency responses, rather than measured time series or Fourier transform data, additional considerations are necessary when feedback or mixing is present, such as those discussed in Ref. [3] using spectral methods. For partially correlated inputs, as quantified by the cross-coherence between inputs and the relative control autospectrum magnitudes, corrections can be applied to condition the data and improve the estimation results. For highly correlated inputs, the indirect approach [4] can be used to retrieve the bare-airframe model from an identified closed-loop model and known control law, or the joint input–output approach can be used to treat the inputs and outputs together as outputs of a separate dynamical system driven by a reference input [4–6]. Despite this additional complexity, a frequency response analysis may be advantageous in some cases, such as for determining a model structure or obtaining starting values for parametric estimation [3].

A different method for frequency response estimation, not using spectral methods, was discussed in Refs. [1,7]. Orthogonal phase-optimized multisine inputs were used to excite the aircraft dynamics by moving multiple control effectors at the same time but with different harmonic frequencies. Frequency responses were then computed by dividing Fourier transforms of measured output and input data evaluated at the harmonic frequencies in the respective inputs. As noted in Ref. [6], the accuracy of these estimates degrades for multiple-input systems when feedback or mixing is present because output data at a particular harmonic frequency can no longer be uniquely attributed to a single input.

In this paper, the frequency response method in Refs. [1,7] is extended to account for the effects of feedback and mixing. The estimation problem was cast as a system of linear algebraic equations. Without feedback or mixing, the system reduces to a fully determined set of equations and the original procedure is recovered. When feedback or mixing is present, the system becomes underdetermined. The determinability was recovered in this case by supplementing equations to the system that interpolate the frequency response among the harmonic frequencies.

The proposed method is useful for estimating frequency responses of multiple-input multiple-output (MIMO) systems, with or without feedback and mixing. Because all control effectors can be excited at the same time, rather than sequentially, flight test durations can be reduced to save time and costs. Frequency responses can be computed in real time to check results and data information during a flight test [7], monitor adaptive control laws, detect sensor and actuator faults [8], or verify stability margins to expedite envelope expansion testing. Postflight analysis of frequency responses can be used for parametric modeling with transfer function or state-space models [9], or can serve as a first pass of the data before an analysis using equation error or output error.

This paper is organized as follows. Section II summarizes the experiment design and the Fourier transform methods. Section III develops the frequency response method using a series of simulation examples based on the T-2 subscale airplane with rate feedback. Section IV demonstrates the method using flight test data for the X-56A airplane, which was flown under closed-loop control and with control surface mixing. Last, Sec. V discusses conclusions. The MATLAB-based software package called System IDentification

Presented as Paper 2019-0009 at the AIAA 2019 SciTech Forum, San Diego, CA, 7–11 January 2019; received 7 May 2019; revision received 16 August 2019; accepted for publication 24 August 2019; published online 24 September 2019.

*Research Engineer, Dynamic Systems and Control Branch, MS 308. Associate Fellow AIAA.

†Research Engineer, Controls and Dynamics Branch, MS 4840D. Member AIAA.

Programs for AirCraft, or SIDPAC [10], was used for the multisine input design, Fourier transforms, and output-error analysis.

II. Experiment Design and Data Analysis

A. Orthogonal Phase-Optimized Multisine Inputs

The orthogonal phase-optimized multisine inputs, subsequently referred to as multisines, were first presented in Refs. [11,12] and are discussed further in Ref. [1]. Multisine inputs are applied over the duration, T, which defines the fundamental frequency $1/T$. Harmonic frequencies k/T are included in the multisines, where k is the integer harmonic number. For frequency response estimation, T is a compromise between meeting operational requirements, achieving a fine frequency resolution, and other factors. The set of n_f included harmonics, K, is selected to span the bandwidth of interest. Good modeling results usually need at least two cycles of each frequency, making $k = 2$ a practical lower limit, although higher values are preferable for disturbance rejection. If lower frequencies or a finer frequency resolution is desired, T should be increased. When designing multisines for multiple inputs, K is divided into the subsets K_j for $j = 1, 2, \ldots, n_u$, each containing n_{f_j} frequencies. Harmonics are typically assigned to these subsets in an alternating manner so that each input has wide coverage over the excitation bandwidth.

Each multisine is constructed as the sum of sinusoids:

$$\mu_j(t) = \sum_{k \in K_j} a_k \sin\left(\frac{2\pi k}{T} t + \phi_k\right) \tag{1}$$

The amplitudes a_k are selected for desired power spectra, and are collectively scaled for desired response levels and signal-to-noise ratios. The phase angles ϕ_k are optimized for minimal relative peak factor (RPF) to keep the aircraft near the target flight condition.

Multisine inputs have many characteristics that are advantageous for frequency response estimation. After initial transient responses decay, multisines elicit steady-state responses, which is the information sought for frequency response estimation. Multisines are analogous to single-sinusoid dwells used in early experiments [13] but are orthogonal and can include many frequencies on many inputs instead of a single frequency on a single input, which reduces the time needed for flight tests. In addition, multisines are symmetric and small-amplitude perturbations that keep the aircraft near the target flight condition, providing good data for linear modeling. One additional feature that is important for the proposed method is that input power is concentrated over a set of discrete and known frequencies.

B. Fourier Transforms

To estimate the frequency responses, measured data are first transformed from the time domain to the frequency domain. The analytical tool for this process is the finite Fourier transform:

$$x(\omega) = \int_0^T x(t) e^{-j\omega t}\, \mathrm{d}t \tag{2}$$

where $x(t)$ is a measured time series, $x(\omega)$ and $x(t)$ are Fourier transform pairs, and ω is the radian frequency.

Equation (2) can be evaluated in several ways. A high-accuracy finite Fourier transform based on the chirp z-transform and cubic interpolation of the measured data can be used in postflight analysis when the entire data record is available [1]. Alternatively, when the sampling rate is much higher than the bandwidth of interest, the Euler approximation

$$x(\omega) \simeq \Delta t \sum_{i=1}^{N} x(t_i) e^{-j\omega t_i} \tag{3}$$

can be used, where Δt is the sampling period and N is the number of samples. This form can be made recursive for each ith data sample in a real-time analysis as

$$x_i(\omega) = \lambda x_{i-1}(\omega) + x(t_i) e^{-j\omega t_i} \Delta t \tag{4}$$

where λ is an exponential forgetting factor ranging between 0 and 1 to systematically discard past data and adapt more quickly to recent information, if desired. The computational simplicity of Eq. (4) enables the analysis of many measurements and many frequencies with low computational requirements.

III. Method Development and Simulation Results

This section develops the frequency response estimation method using a series of simulation examples based on the short-period dynamics of the T-2 airplane having two inputs, two states, and two outputs. First, the simulation model and multisine inputs are presented. Second, the model was simulated in the open-loop configuration, and frequency responses were estimated using the basic approach introduced in Refs. [1,7]. Next, pitch rate was fed back to one input, and the inadequacy of the basic approach in this situation is discussed, as well as solution strategies. Pitch rate was then fed back to both inputs and the general approach for frequency response estimation with arbitrary feedback and mixing is formalized. Afterward, real-time estimation and other characteristics of the method are discussed.

A. T-2 Short-Period Simulation

The T-2 airplane, shown in Fig. 1, is a dynamically scaled 5.5% version of a generic commercial transport aircraft and has been used extensively for flight test research. Its short-period dynamics were selected for investigation because they are relatively small in dimension but exhibit the relevant issues when identifying MIMO bare-airframe dynamics from closed-loop data using frequency responses. Table 1 lists parameters for the aircraft geometry and nominal mass properties. The reference condition was straight and level flight at 1270 ft altitude, 130 ft/s true airspeed, and 4.0 deg angle of attack.

The two inputs were the symmetric pairs of outboard and inboard elevator surface deflections, δ_{eo} and δ_{ei}, and the two outputs were pitch rate, q, and vertical acceleration at the center of mass, a_z. The transfer function matrix representation of the bare-airframe dynamics was

$$\boldsymbol{H}(s) = \begin{bmatrix} \dfrac{q(s)}{\delta_{eo}(s)} & \dfrac{q(s)}{\delta_{ei}(s)} \\ \dfrac{a_z(s)}{\delta_{eo}(s)} & \dfrac{a_z(s)}{\delta_{ei}(s)} \end{bmatrix} = \frac{\begin{bmatrix} -18.1s - 36.0 & -18.1s - 36.0 \\ -0.38s^2 - 0.40s + 146 & -0.38s^2 - 0.40s + 146 \end{bmatrix}}{s^2 + 5.13s + 35.1} \tag{5}$$

where the corresponding nondimensional stability and control derivatives, given in Table 2, were identified from flight test data using the equation-error method in the frequency domain [1].

Fig. 1 T-2 airplane (credit: NASA Langley Research Center).

Table 1 T-2 aircraft geometry and nominal mass properties

Parameter	Value	Unit
$\bar{c}$	0.92	ft
b	6.85	ft
S	5.90	ft^2
m	1.59	slug
I_{xx}	1.18	slug-ft^2
I_{yy}	4.52	slug-ft^2
I_{zz}	5.53	slug-ft^2
I_{xz}	0.21	slug-ft^2

Table 2 Stability and control derivatives for the T-2 simulation

Parameter	Value
C_{Z_α}	−3.89
C_{Z_q}	−5.17
$C_{Z_{\delta_{eo}}}$	−0.17
$C_{Z_{\delta_{ei}}}$	−0.17
C_{m_α}	−1.30
C_{m_q}	−37.1
$C_{m_{\delta_{eo}}}$	−0.80
$C_{m_{\delta_{ei}}}$	−0.80

The simulated bare-airframe model had damping ratio $\zeta = 0.43$ and natural frequency $\omega_n = 5.9$ rad/s (0.94 Hz).

Figure 2 shows a block diagram of a pitch-rate feedback control architecture surrounding the bare airframe model, which was simulated with a fixed-step integration at 50 Hz. The inputs u_1 and u_2 were δ_{eo} and δ_{ei}, and the outputs y_1 and y_2 were q and a_z. Each of these four signals passed through sensor dynamics, S, and was added to Gaussian white noise sequences, v, to model the measurements, which are denoted with the m subscript. The sensor dynamics were negligible ($S = 1$) but were included to discuss their effects in the next section. Measurement noise levels are listed in Table 3 and were identified from flight test data in calm air. Actuator models were

$$A_j(s) = \frac{u_j(s)}{u_{j_c}(s)} = \frac{18.8}{s + 18.8} e^{-0.01s} \tag{6}$$

where the actuator commands, u_{j_c}, consisted of inputs from the pilot, η, multisine inputs, and pitch-rate feedback signals through the control gains C_{11} and C_{21}. The blue and red colors for the multisine excitations are used throughout the simulation examples to distinguish between the two sets of harmonic frequencies.

Table 4 parameterizes the multisines used for all the simulation examples. The duration was $T = 20$ s and the bandwidth of excitation was between 0.2 and 1.55 Hz, in 0.05 Hz increments, which resulted in 28 harmonic frequencies or 14 frequencies per input. The amplitude spectra had equal power at each frequency and were scaled to realistic values used in flight tests.

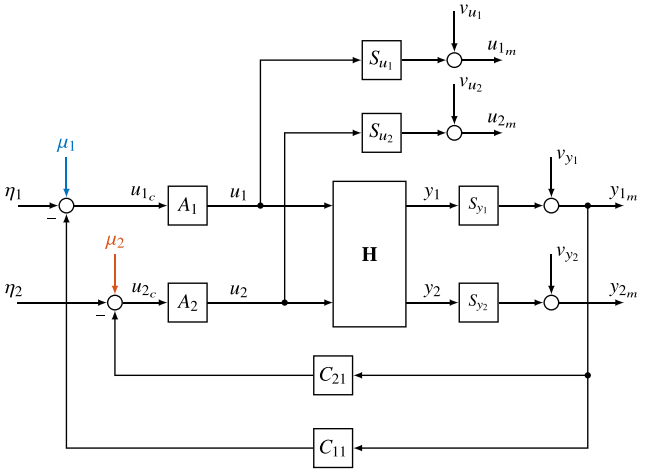

Fig. 2 Block diagram for the T-2 simulation.

Table 3 Measurement noise levels for the T-2 simulation

Measurement	Standard deviation	Unit
δ_{eo}, δ_{ei}	0.031	deg
q	0.41	deg/s
a_z	0.010	g

Table 4 Multisine design parameters for the T-2 simulation ($T = 20$ s)

Outboard elevator, K_1			Inboard elevator, K_2		
RPF = 1.01			RPF = 1.06		
a_k, deg	k	ϕ_k, rad	a_k, deg	k	ϕ_k, rad
0.53	4	0.62	0.53	5	4.94
0.53	6	5.16	0.53	7	3.26
0.53	8	1.68	0.53	9	2.09
0.53	10	6.22	0.53	11	2.91
0.53	12	2.69	0.53	13	2.58
0.53	14	3.49	0.53	15	0.26
0.53	16	3.51	0.53	17	4.53
0.53	18	4.24	0.53	19	2.70
0.53	20	3.28	0.53	21	3.23
0.53	22	1.97	0.53	23	4.14
0.53	24	1.55	0.53	25	5.53
0.53	26	4.20	0.53	27	2.70
0.53	28	5.37	0.53	29	6.26
0.53	30	2.68	0.53	31	1.32

B. Open Loop

The simulation model was first run in the open-loop configuration without feedback control, that is, $C_{11} = C_{21} = 0$, and measurements are shown in Fig. 3a. The control surface deflections, shown in the first two plots, had a correlation coefficient of 0. The signal-to-noise ratios for all signals were high at above 17 (computed using a smoothing technique [1]), and the response perturbation magnitudes were similar to flight test data used to obtain good linear modeling results.

Fourier transform magnitudes of the measurements are shown in Fig. 3b. The transforms were only evaluated at the 28 harmonic frequencies because only those frequencies contained significant power in the steady-state responses, due to linearity of the system. For these plots, blue circles indicate harmonic frequencies used for δ_{eo}, and red squares indicate harmonic frequencies used for δ_{ei}. Note that, for this open-loop case, the measured control surface deflections each contained power for a single set of unique harmonic frequencies—this will not be the case in later examples with feedback and mixing.

To compute frequency response estimates of the bare-airframe dynamics from these data, each of the n_y outputs can be expanded using transfer function algebra as

$$\begin{aligned} y_{i_m} &= S_{y_i} y_i + v_{y_i} \\ &= S_{y_i}[H_{i1}u_1 + H_{i2}u_2] + v_{y_i} \\ &= S_{y_i}[H_{i1}S_{u_1}^{-1}(u_{1_m} - v_{u_1}) + H_{i2}S_{u_2}^{-1}(u_{2_m} - v_{u_2})] + v_{y_i} \end{aligned} \tag{7}$$

which shows contributions of the sensors, measurements, and bare-airframe frequency responses. Measurement noise or error in the sensor models can degrade the accuracy of frequency response estimates. However, sensors can typically be characterized well and are usually selected to have negligible dynamics in the bandwidth of interest. Furthermore, good multisine designs achieve high signal-to-noise ratios at the harmonic frequencies. Although measurement noise and sensor dynamics may be considered in the analysis, these

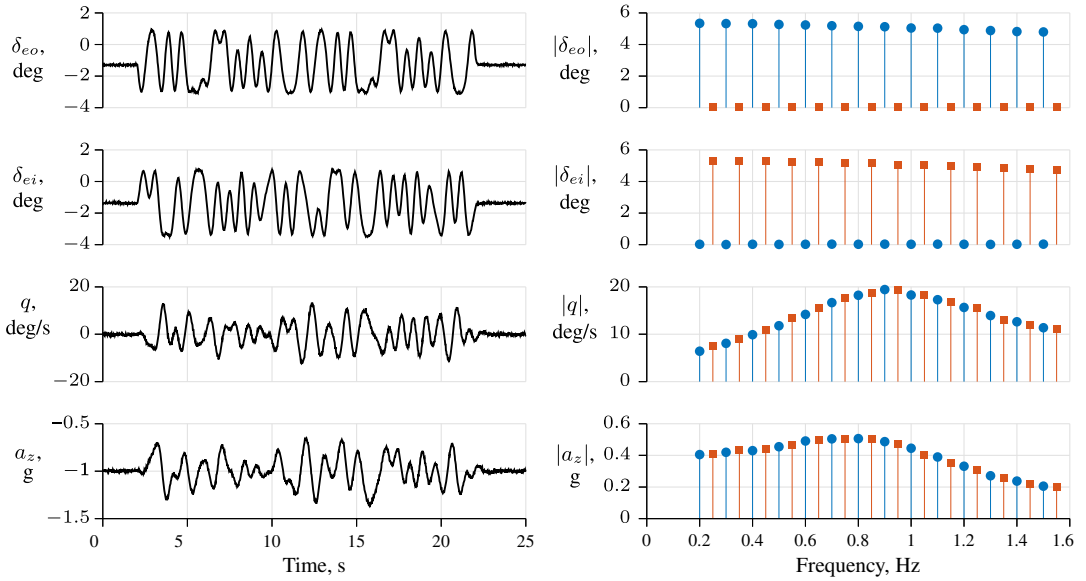

a) Time histories **b) Fourier transform magnitudes**

Fig. 3 T-2 simulation data in open-loop configuration.

effects can often be neglected (which was done in the remaining development) so that $y_{i_m} \simeq y_i$, $u_{j_m} \simeq u_j$, and $S_{y_i} = S_{u_j} = 1$, simplifying Eq. (7) to

$$y_i = H_{i1}u_1 + H_{i2}u_2 \tag{8}$$

Evaluating Eq. (8) at each harmonic frequency results in a system of linear equations of the form $\boldsymbol{b} = \boldsymbol{A}\boldsymbol{x}$, which is a fundamental problem of linear algebra. For the open-loop case, $\boldsymbol{A}$ has dimensions $(n_y \cdot n_f) \times (n_y \cdot n_u \cdot n_f)$ and is not a square matrix. The system can be partitioned as

$$\begin{bmatrix} \boldsymbol{b}_1 \\ \boldsymbol{b}_2 \end{bmatrix} = \begin{bmatrix} \boldsymbol{A}_{11} & \boldsymbol{0} \\ \boldsymbol{0} & \boldsymbol{A}_{22} \end{bmatrix} \begin{bmatrix} \boldsymbol{x}_1 \\ \boldsymbol{x}_2 \end{bmatrix} \tag{9}$$

Letting vectors $\boldsymbol{\omega}_1$ and $\boldsymbol{\omega}_2$ represent the respective frequencies in K_1 and K_2, the $(n_y \cdot n_{f_j}) \times 1$ partitions

$$\boldsymbol{b}_1 = \begin{bmatrix} y_1(\boldsymbol{\omega}_1) \\ y_2(\boldsymbol{\omega}_1) \end{bmatrix}, \qquad \boldsymbol{b}_2 = \begin{bmatrix} y_1(\boldsymbol{\omega}_2) \\ y_2(\boldsymbol{\omega}_2) \end{bmatrix} \tag{10}$$

are the measured output Fourier transforms, evaluated at the two sets of harmonic frequencies. Similarly, the $(n_y \cdot n_u \cdot n_{f_j}) \times 1$ partitions

$$\boldsymbol{x}_1 = \begin{bmatrix} H_{11}(\boldsymbol{\omega}_1) \\ H_{21}(\boldsymbol{\omega}_1) \\ H_{12}(\boldsymbol{\omega}_1) \\ H_{22}(\boldsymbol{\omega}_1) \end{bmatrix}, \qquad \boldsymbol{x}_2 = \begin{bmatrix} H_{11}(\boldsymbol{\omega}_2) \\ H_{21}(\boldsymbol{\omega}_2) \\ H_{12}(\boldsymbol{\omega}_2) \\ H_{22}(\boldsymbol{\omega}_2) \end{bmatrix} \tag{11}$$

are evaluations of the bare-airframe frequency responses at $\boldsymbol{\omega}_1$ and $\boldsymbol{\omega}_2$. Lastly, the $(n_y \cdot n_{f_j}) \times (n_y \cdot n_u \cdot n_{f_j})$ partitions

$$\boldsymbol{A}_{11} = \begin{bmatrix} d\{u_1(\boldsymbol{\omega}_1)\} & \boldsymbol{0} & d\{u_2(\boldsymbol{\omega}_1)\} & \boldsymbol{0} \\ \boldsymbol{0} & d\{u_1(\boldsymbol{\omega}_1)\} & \boldsymbol{0} & d\{u_2(\boldsymbol{\omega}_1)\} \end{bmatrix} \tag{12a}$$

$$\boldsymbol{A}_{22} = \begin{bmatrix} d\{u_1(\boldsymbol{\omega}_2)\} & \boldsymbol{0} & d\{u_2(\boldsymbol{\omega}_2)\} & \boldsymbol{0} \\ \boldsymbol{0} & d\{u_1(\boldsymbol{\omega}_2)\} & \boldsymbol{0} & d\{u_2(\boldsymbol{\omega}_2)\} \end{bmatrix} \tag{12b}$$

are assembled from the measured input Fourier transforms, where $d\{.\}$ constructs a diagonal matrix from the argument.

The frequency responses at the harmonic frequencies are computed by solving the system for $\boldsymbol{x}$. Normally, Eq. (9) is underdetermined because there are n_u times as many unknowns as there are equations. However, in the open-loop case with negligible pilot input,

$$u_1(\boldsymbol{\omega}_2) = A_1(\boldsymbol{\omega}_2)\mu_1(\boldsymbol{\omega}_2) = \boldsymbol{0} \tag{13a}$$

$$u_2(\boldsymbol{\omega}_1) = A_2(\boldsymbol{\omega}_1)\mu_2(\boldsymbol{\omega}_1) = \boldsymbol{0} \tag{13b}$$

by definition and as seen in Figs. 2 and 3b. Applying this substitution nulls half the elements along diagonals of $\boldsymbol{A}_{11}$ and $\boldsymbol{A}_{22}$, reducing the system to

$$\begin{bmatrix} y_1(\boldsymbol{\omega}_1) \\ y_2(\boldsymbol{\omega}_1) \\ y_1(\boldsymbol{\omega}_2) \\ y_2(\boldsymbol{\omega}_2) \end{bmatrix} = \begin{bmatrix} d\{u_1(\boldsymbol{\omega}_1)\} & \boldsymbol{0} & \boldsymbol{0} & \boldsymbol{0} \\ \boldsymbol{0} & d\{u_1(\boldsymbol{\omega}_1)\} & \boldsymbol{0} & \boldsymbol{0} \\ \boldsymbol{0} & \boldsymbol{0} & d\{u_2(\boldsymbol{\omega}_2)\} & \boldsymbol{0} \\ \boldsymbol{0} & \boldsymbol{0} & \boldsymbol{0} & d\{u_2(\boldsymbol{\omega}_2)\} \end{bmatrix} \times \begin{bmatrix} H_{11}(\boldsymbol{\omega}_1) \\ H_{21}(\boldsymbol{\omega}_1) \\ H_{12}(\boldsymbol{\omega}_2) \\ H_{22}(\boldsymbol{\omega}_2) \end{bmatrix} \tag{14}$$

in which the reduced $\boldsymbol{A}$ has the square dimensions $(n_y \times n_f) \times (n_y \times n_f)$. The decoupled, fully determined system has the solution $\boldsymbol{x} = \boldsymbol{A}^{-1}\boldsymbol{b}$, or

$$\begin{bmatrix} H_{11}(\boldsymbol{\omega}_1) \\ H_{21}(\boldsymbol{\omega}_1) \\ H_{12}(\boldsymbol{\omega}_2) \\ H_{22}(\boldsymbol{\omega}_2) \end{bmatrix} = \begin{bmatrix} d\{\frac{1}{u_1(\boldsymbol{\omega}_1)}\} & \boldsymbol{0} & \boldsymbol{0} & \boldsymbol{0} \\ \boldsymbol{0} & d\{\frac{1}{u_1(\boldsymbol{\omega}_1)}\} & \boldsymbol{0} & \boldsymbol{0} \\ \boldsymbol{0} & \boldsymbol{0} & d\{\frac{1}{u_2(\boldsymbol{\omega}_2)}\} & \boldsymbol{0} \\ \boldsymbol{0} & \boldsymbol{0} & \boldsymbol{0} & d\{\frac{1}{u_2(\boldsymbol{\omega}_2)}\} \end{bmatrix} \begin{bmatrix} y_1(\boldsymbol{\omega}_1) \\ y_2(\boldsymbol{\omega}_1) \\ y_1(\boldsymbol{\omega}_2) \\ y_2(\boldsymbol{\omega}_2) \end{bmatrix} \tag{15}$$

More generally, this solution is also expressed as

$$H_{ij}(\boldsymbol{\omega}_j) = \frac{y_i(\boldsymbol{\omega}_j)}{u_j(\boldsymbol{\omega}_j)} \tag{16}$$

which is the ratio of output and input Fourier transforms at the frequencies contained in the input. This development is a different way of viewing the *basic approach* for frequency response

estimation presented in Refs. [1,7]. Equation (16) is applied for each harmonic in each input, and the frequency response matrix is computed at the corresponding frequencies.

Computing frequency responses in this manner has several advantages. The analysis is straightforward and does not require tuning or using engineering judgment to select parameters in the calculations. It is applicable to MIMO systems and is simple enough to run in real time during flight with low computational resources. For high signal-to-noise ratios and sufficient durations, these estimates of the frequency response are accurate and unbiased [4,14]. However, computerized excitations are necessary, and additional pilot inputs should be small to keep from adding power within the excitation bandwidth. These are not usually problematic because research aircraft are often outfitted with a flight control computer and because the multisines are small-perturbation inputs that are symmetric about zero. Also, flight testing should be conducted in calm air because atmospheric turbulence creates transient responses and acts as an unmeasured input to the system. Furthermore, adequate signal-to-noise ratios, steady-state and small-perturbation response data, and minimal changes in the bare-airframe dynamics (such as from fuel burn or airspeed variation) are needed for accurate frequency response estimates.

Figure 4 shows the resulting frequency response estimates as Bode plots. The left column, containing blue circles, represents frequency responses of q and a_z to input δ_{eo} and were computed at harmonics in K_1. Likewise, the right column, containing red squares, represents the frequency responses of q and a_z to input δ_{ei} and were computed at harmonics in K_2. The true frequency responses of the bare-airframe simulation model were computed from Eq. (5) and are shown as solid black lines. The estimates were in excellent agreement with the true frequency responses, with maximum Bode magnitude and phase errors less than 0.4 dB and 2.5 deg, respectively.

Overlaying the true frequency responses in Fig. 4 are dashed purple lines, which are the results of an output-error analysis [1] to estimate stability and control derivatives in a state-space representation of Eq. (5) that best match the model output Fourier transforms to measured frequency-domain output data in a maximum likelihood sense. These frequency responses are practically indistinguishable from the true curves. The output-error analysis was included in the simulation examples to establish a baseline for comparison later in Sec. IV, where flight test data were analyzed. When applying output error in this way, it is important that the input correlation coefficients remain less than about 0.9 in absolute value, which was the case for all results shown in this paper.

C. Single-Loop Closure

In this second simulation example, q was fed back to δ_{ei} with $C_{11} = 0$ and $C_{21} = -0.2$. The closed-loop short-period mode had damping ratio 0.70 and natural frequency 8.0 rad/s (1.3 Hz). This type of stability augmentation has been used to artificially degrade stability and control characteristics of the T-2 airplane in research flight tests.

Simulated time histories and Fourier transforms of measurements for this case are shown in Fig. 5. Data for δ_{eo} were the same as in the previous example, whereas δ_{ei} contained additional contributions from the feedback, particularly near the short-period resonance. The feedback increased the input correlation coefficient from 0 to 0.4, reduced the response amplitudes, and resulted in harmonic frequency content on δ_{ei} from both K_1 and K_2.

To compute frequency responses from these data, the output responses can be written as in Eq. (8). From the block diagram for this example, $u_1(\omega_2) = \mathbf{0}$ as before, whereas

$$\begin{aligned} u_2(\omega_1) &= A_2(\omega_1)[\mu_2(\omega_1) - C_{21}(\omega_1)y_1(\omega_1)] \\ &= -A_2(\omega_1)C_{21}(\omega_1)y_1(\omega_1) \end{aligned} \tag{17}$$

which is nonzero because the steady-state outputs contained power at both sets of harmonic frequencies, as seen in Fig. 5b. In this case, the frequency responses from u_2 (containing feedback) to y_1 and y_2 were ratios of Fourier transforms, as in Eq. (16) for the open-loop configuration. However, the frequency responses from u_1 (not containing feedback) to y_1 and y_2 were

$$H_{i1}(\omega_1) = \frac{y_i(\omega_1)}{u_1(\omega_1)} - \frac{H_{i2}(\omega_1)u_2(\omega_1)}{u_1(\omega_1)} \tag{18}$$

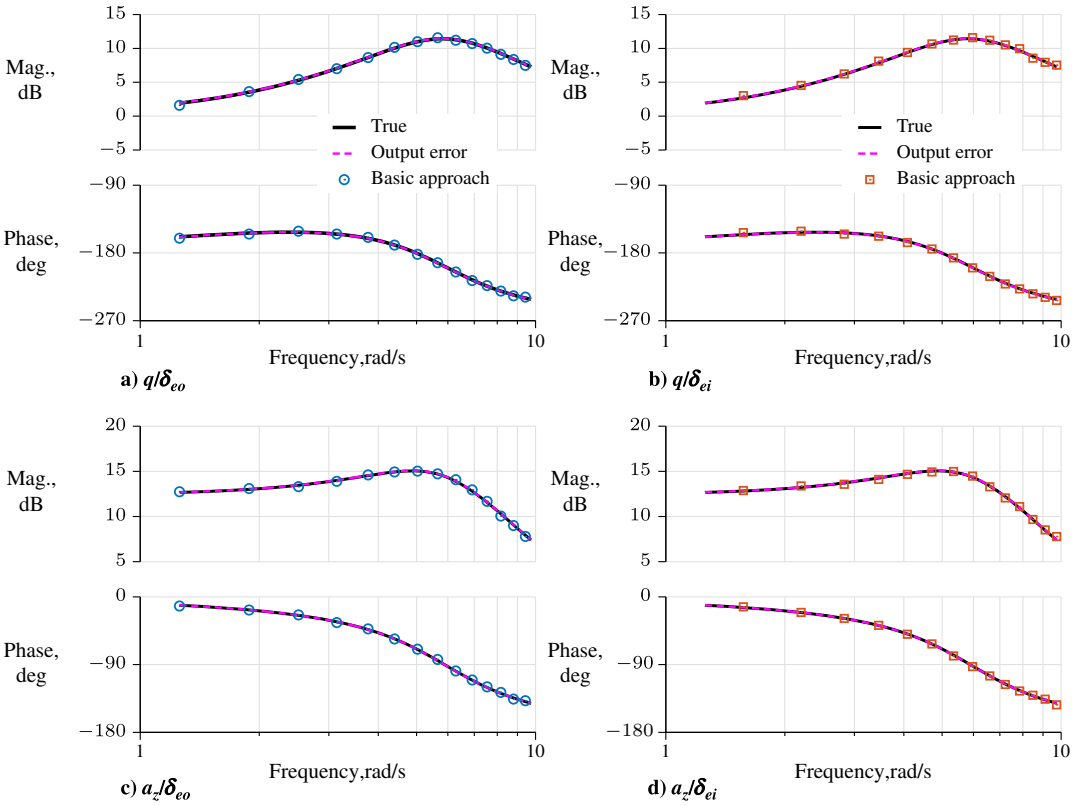

Fig. 4 Frequency response estimates for the T-2 simulation in open-loop configuration.

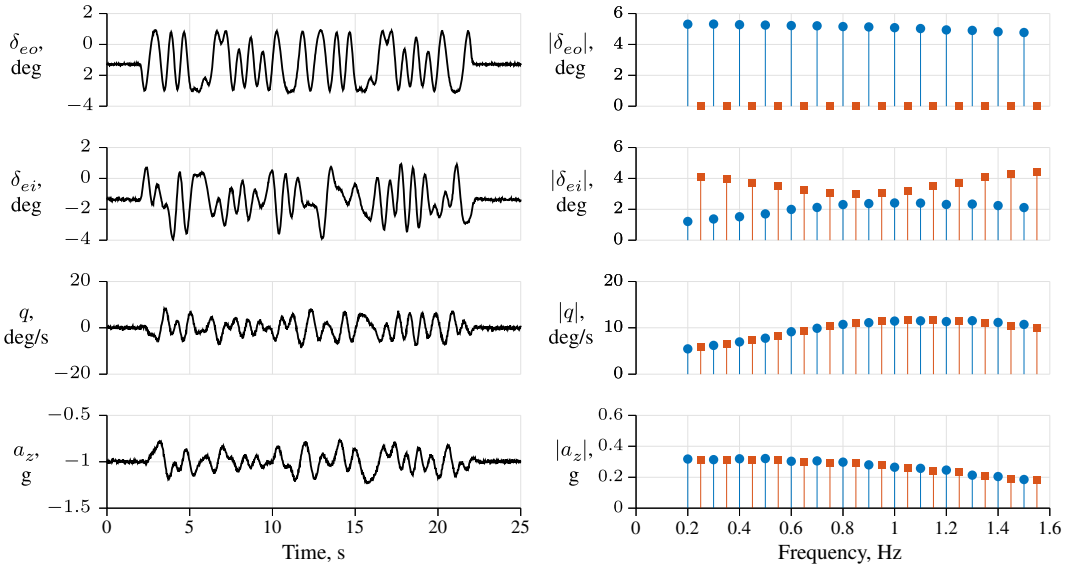

a) Time histories **b) Fourier transform magnitudes.**

Fig. 5 T-2 simulation data with single-loop closure.

and had more terms than in the open-loop case. Therefore, $H_{i2}(\boldsymbol{\omega}_2)$ can be calculated using the basic approach, but $H_{i1}(\boldsymbol{\omega}_1)$ needs more information. Note that it is the frequency response with the input *not* containing feedback that is in error when estimated using the basic approach. Also note that, as $C_{21} \to 0$, $u_2(\boldsymbol{\omega}_1) \to 0$ in the steady state and the basic approach is recovered.

There are several strategies to compute $H_{i1}(\boldsymbol{\omega}_1)$. Multiple maneuvers using single-input excitations at the same target flight condition could be combined. Alternatively, the data for $H_{i2}(\boldsymbol{\omega}_2)$ could be fit with a parametric model [9], such as a transfer function, and then evaluated at the frequencies $\boldsymbol{\omega}_1$. As another option, $H_{i2}(\boldsymbol{\omega}_2)$ could be interpolated for the frequencies $\boldsymbol{\omega}_1$ by recasting the system of linear equations as

$$\begin{bmatrix} \boldsymbol{b}_1 \\ \boldsymbol{b}_2 \\ \boldsymbol{0} \end{bmatrix} = \begin{bmatrix} \boldsymbol{A}_{11} & \boldsymbol{0} \\ \boldsymbol{0} & \boldsymbol{A}_{22} \\ \boldsymbol{A}_{31} & \boldsymbol{A}_{32} \end{bmatrix} \begin{bmatrix} \boldsymbol{x}_1 \\ \boldsymbol{x}_2 \end{bmatrix} \tag{19}$$

where the third partitioned row specifies the interpolation. For this example and using linear interpolation, half the elements in $\boldsymbol{A}_{22}$ are nulled, $\boldsymbol{A}_{31}$ has values of $1/2$ along two of the diagonals, and $\boldsymbol{A}_{32}$ has values of -1 along the diagonal. The interpolation equations in this *general approach* add enough information to make the reduced system fully determined so that a solution can be computed.

Frequency response estimates using the simulation data are shown in Fig. 6. Results from an output-error analysis matched the true frequency responses. For the responses from δ_{ei}, estimates computed

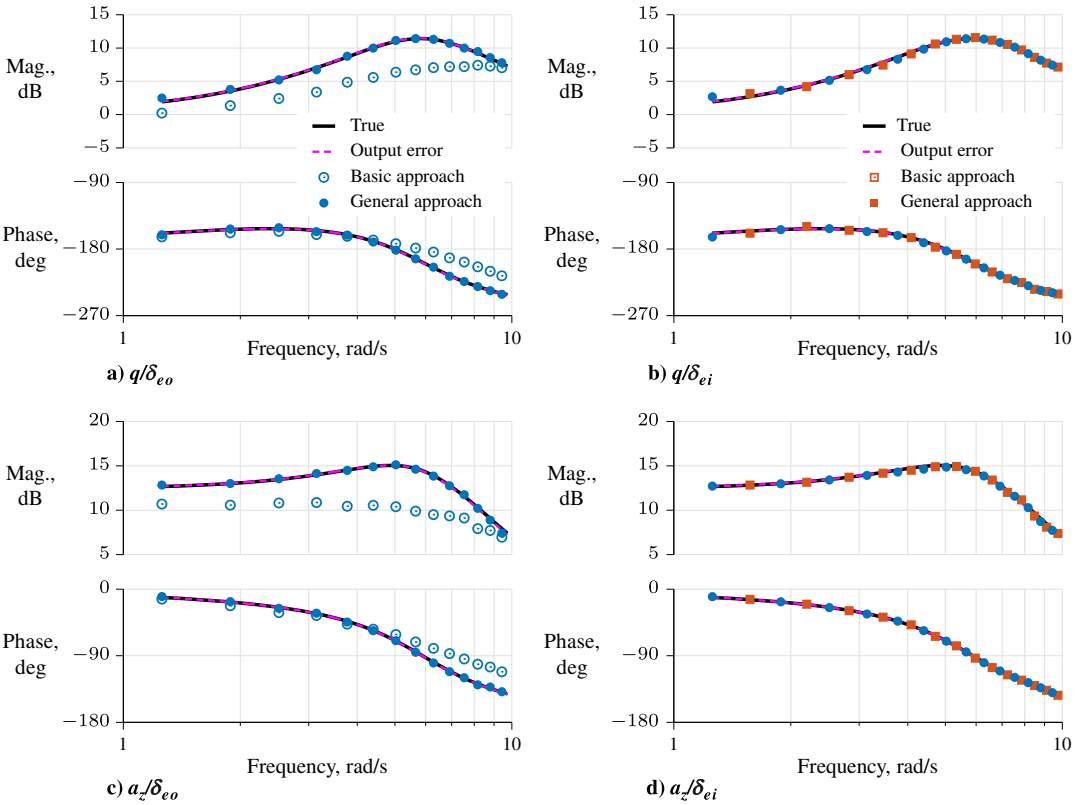

a) q/δ_{eo} **b) q/δ_{ei}**

c) a_z/δ_{eo} **d) a_z/δ_{ei}**

Fig. 6 Frequency response estimates for T-2 simulation with single-loop closure.

with the basic approach matched those with the general approach (shown as solid markers) and were within 0.5 dB and 3.0 deg of the true frequency responses. Additional frequency response estimates at frequencies in K_1 resulted from the interpolation. For the responses from δ_{eo}, estimates computed using the basic approach had errors up to 4.7 dB and 29.0 deg, which increased the apparent damping ratio and natural frequency. This discrepancy was demonstrated in Ref. [6] and is the result of neglecting the second term on the right side of Eq. (18). Estimates computed with the general approach agreed with the true bare-airframe frequency responses to within 0.5 dB and 3.0 deg, similar to frequency responses from δ_{ei} and the open-loop example.

D. Multiple-Loop Closures

In this third simulation example, q was fed back to both δ_{eo} and δ_{ei}, with $C_{11} = C_{21} = -0.1$. The closed-loop short-period mode had damping ratio 0.68 and natural frequency 7.7 rad/s (1.2 Hz). This stability augmentation achieved approximately the same closed-loop dynamics as the previous example, but distributed the feedback evenly among the two inputs.

Simulated measurements for this case are shown in Fig. 7. The input correlation coefficient was 0.3, which was less than in the previous simulation example because the feedback gain was lower in value, even though both inputs contained feedback. The measured outputs had approximately the same magnitudes as the previous case because roughly the same closed-loop dynamics were achieved. The inputs contained power at harmonic frequencies in both K_1 and K_2, due to the feedback.

To solve for the frequency responses, the output measurements were again expanded as in Eq. (8). In this case

$$\begin{aligned} u_1(\boldsymbol{\omega}_2) &= A_1(\boldsymbol{\omega}_2)[\mu_1(\boldsymbol{\omega}_2) - C_{11}(\boldsymbol{\omega}_2)y_1(\boldsymbol{\omega}_2)] \\ &= -A_1(\boldsymbol{\omega}_2)C_{11}(\boldsymbol{\omega}_2)y_1(\boldsymbol{\omega}_2) \end{aligned} \tag{20a}$$

$$\begin{aligned} u_2(\boldsymbol{\omega}_1) &= A_2(\boldsymbol{\omega}_1)[\mu_2(\boldsymbol{\omega}_1) - C_{21}(\boldsymbol{\omega}_1)y_1(\boldsymbol{\omega}_1)] \\ &= -A_2(\boldsymbol{\omega}_1)C_{21}(\boldsymbol{\omega}_1)y_1(\boldsymbol{\omega}_1) \end{aligned} \tag{20b}$$

which were both nonzero. The frequency responses were then

$$H_{i1}(\boldsymbol{\omega}_1) = \frac{y_i(\boldsymbol{\omega}_1)}{u_1(\boldsymbol{\omega}_1)} - \frac{H_{i2}(\boldsymbol{\omega}_1)u_2(\boldsymbol{\omega}_1)}{u_1(\boldsymbol{\omega}_1)} \tag{21a}$$

$$H_{i2}(\boldsymbol{\omega}_2) = \frac{y_i(\boldsymbol{\omega}_2)}{u_2(\boldsymbol{\omega}_2)} - \frac{H_{i1}(\boldsymbol{\omega}_2)u_1(\boldsymbol{\omega}_2)}{u_2(\boldsymbol{\omega}_2)} \tag{21b}$$

Unlike the previous example, one frequency response cannot be computed first and then substituted into the remaining equation; rather, more information must be obtained and the entire set of unknown frequency responses solved simultaneously. In the limit as both control gains decrease, the basic approach is again recovered.

Applying the same interpolation strategy, the system of linear equations is expanded as

$$\begin{bmatrix} \boldsymbol{b}_1 \\ \boldsymbol{b}_2 \\ \boldsymbol{0} \\ \boldsymbol{0} \end{bmatrix} = \begin{bmatrix} \boldsymbol{A}_{11} & \boldsymbol{0} \\ \boldsymbol{0} & \boldsymbol{A}_{22} \\ \boldsymbol{A}_{31} & \boldsymbol{A}_{32} \\ \boldsymbol{A}_{41} & \boldsymbol{A}_{42} \end{bmatrix} \begin{bmatrix} \boldsymbol{x}_1 \\ \boldsymbol{x}_2 \end{bmatrix} \tag{22}$$

The fourth partitioned row interpolates $H_{i1}(\boldsymbol{\omega}_2)$ from $H_{i1}(\boldsymbol{\omega}_1)$, similar to the third partitioned row. The interpolated equations make $\boldsymbol{A}$ a square matrix without eliminating any variables or reducing the system.

The frequency response estimates are shown in Fig. 8. Results from the output-error analysis again matched the true frequency responses. Because of the interpolation, estimates computed using the general approach were available for all responses at all 28 harmonic frequencies. Estimates computed with the basic approach had errors up to 2.7 dB and 15.5 deg, which again increased the apparent damping ratio and natural frequency. In comparison to the previous example, the errors were approximately halved and evenly distributed between the two groups of frequency responses because the two inputs were used equally to achieve the same closed-loop dynamics. Estimates computed with the general approach were more accurate and had errors less than 0.5 dB and 2.8 deg, similar to the two previous examples.

E. Real-Time Estimation with Multiple-Loop Closures

To compute frequency responses in real time, recursive Fourier transforms are updated for new data using Eq. (4) and frequency responses are calculated using Eq. (22). Although $\boldsymbol{A}$ can become large for many inputs, outputs, and frequencies, there are several aspects that reduce the computational burden for real-time computation. First, for a given experimental setup, the interpolation matrices $\boldsymbol{A}_{31}$, $\boldsymbol{A}_{32}$, $\boldsymbol{A}_{41}$, and $\boldsymbol{A}_{42}$ are computed and assembled once, before any data are collected, and remain fixed over time. As data are recorded, only $\boldsymbol{b}_1$, $\boldsymbol{b}_2$, $\boldsymbol{A}_{11}$, and $\boldsymbol{A}_{22}$ are updated from the

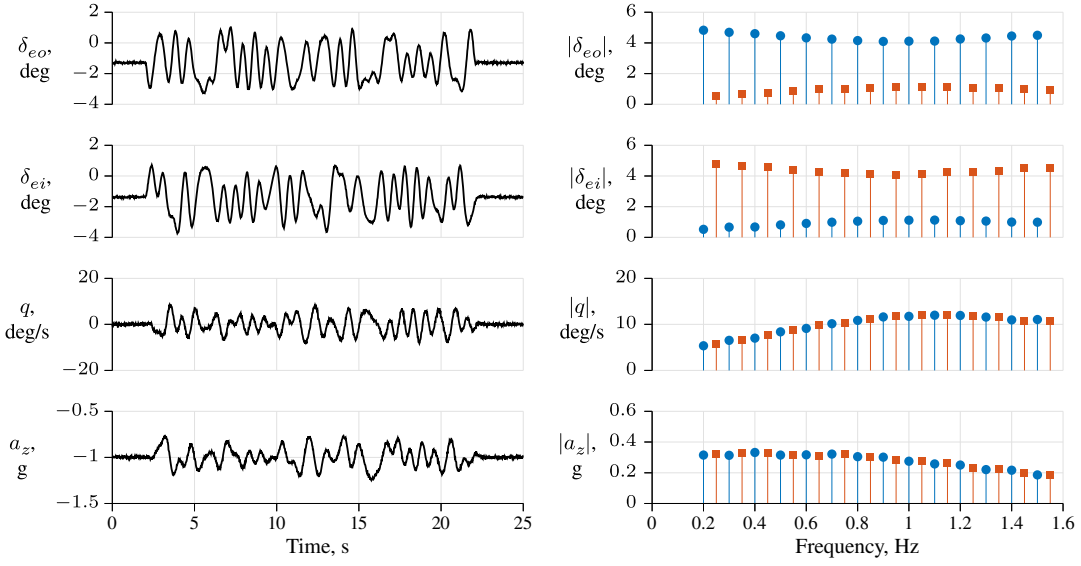

a) Time histories b) Fourier transform magnitudes

Fig. 7 T-2 simulation data with multiple-loop closures.

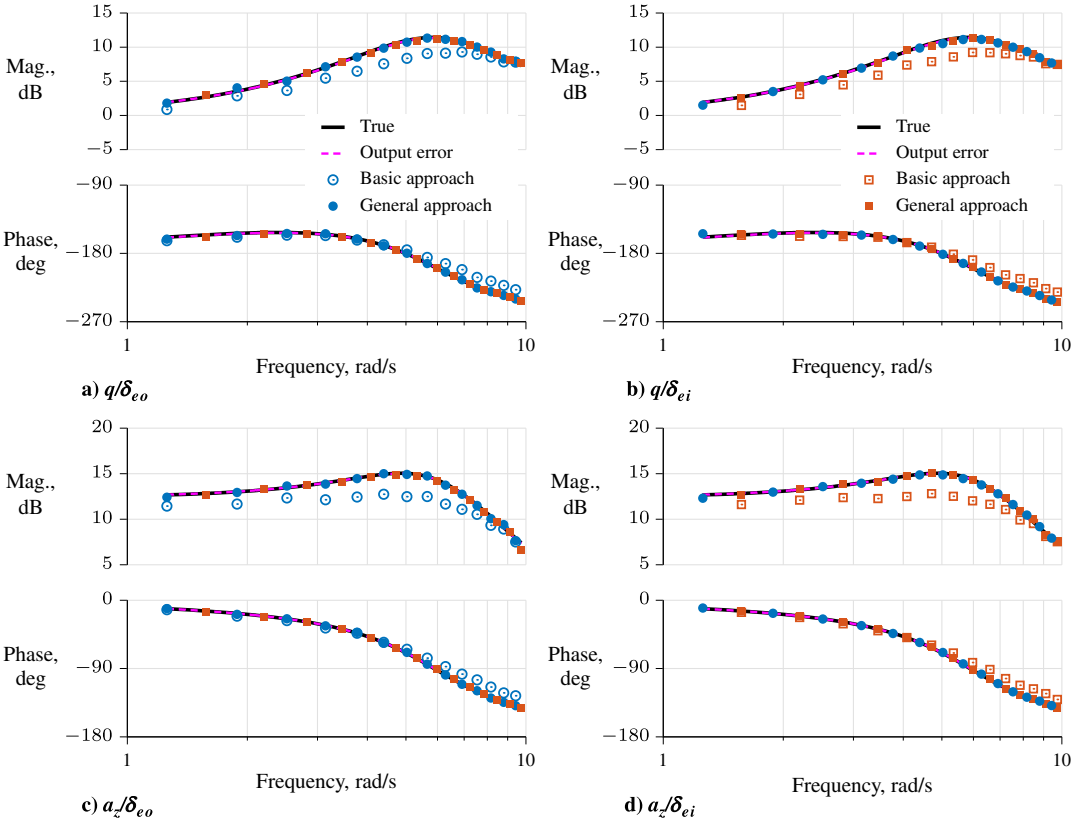

Fig. 8 Frequency response estimates for T-2 simulation with multiple-loop closures.

measurements. Second, although Fourier transforms need to be computed at a sufficiently high rate, frequency responses can often be updated at a slower rate. For example, Fourier transforms describing rigid-body dynamics could run at 25 Hz, but then frequency responses can be computed and displayed at 1 Hz. Last, $\boldsymbol{A}$ mostly contains nonzero elements along diagonals of the matrix, and so efficient numerical routines can exploit this sparsity to significantly reduce computation time when many inputs, outputs, and frequencies are considered.

The data from the previous example were processed recursively. On average, about 0.1% of the 0.02 s sample period was needed to transform the data into the frequency domain, and 20% of the sample period was needed to solve for the frequency responses using a standard laptop computer running MATLAB, which left about 80% of the sample period free. The evolution of the a_z/δ_{eo} frequency response is shown in Figs. 9a and 9b. Frequency responses were computed after the excitation onset at times corresponding to half and whole cycles of oscillation to minimize partial-period errors in the Fourier transform. As more data were collected, the estimates converged on the final values, which are also shown in the plots at the end of the maneuver. There was more oscillation in the estimates at higher frequencies than lower frequencies due to lower signal-to-noise ratios and because these estimates were updated more frequently. Transient responses contributed to the errors near the start of the excitation, when there was little steady-state information, but did not significantly affect the estimates near the end of the maneuver when the excitation ended. Average errors (taken for a particular time sample over the 28 harmonic frequencies) in the Bode magnitude and phase over time, shown in Fig. 9c, generally converged after 10 s of excitation.

F. Discussion

Similar to the basic approach, the general approach for frequency response estimation is procedural and does not require tuning parameters or engineering judgment. Because the bare-airframe inputs are measured, no knowledge of the internal control law or mixing scheme is necessary. Under good testing conditions (calm air, high signal-to-noise ratio, steady-state response data, minimal changes in the bare-airframe dynamics), good results can be obtained, with errors decreasing as more data are obtained.

Because the proposed method is based on Fourier transform data, rather than spectral density estimates, the coherence function (which quantifies the linearity of the input–output process based on the measured data) typically used to assess the quality of an empirical frequency response estimate is meaningless. However, when the measurement noise is white and Gaussian, the resulting frequency responses computed using the basic approach will also have these characteristics [7,9]. Results of running the simulation and analysis discussed in Sec. III.D 500 times with different noise sequences, shown in Fig. 10 for the a_z/δ_{eo} frequency response, demonstrate that this is also true for the general method. The real and imaginary parts of the frequency response are shown for the true system and the estimates. The markers are the mean estimates from the runs, averaged at the same frequencies, and the error bars reflect the 2σ variation. The estimates were in close agreement with the true frequency response, had approximately the same scatter over frequency, and appeared normally distributed. Note that, when estimates are shown as a Bode plot, instead of real and imaginary parts, the errors vary in frequency due to the nonlinear transforms involved in computing the magnitude and phase components from the complex-valued frequency responses [9].

The effect of the augmentation level on the accuracy of the method was also examined. Figure 11 shows the mean and 2σ variation of the average error (taken over the 28 harmonic frequencies) in the Bode magnitude and phase estimates for a_z/δ_{eo} as a function of the control gains $C_{11} = C_{21}$, for 500 simulation runs each. Larger control gains were not investigated because the closed-loop natural frequency would significantly shift relative to the excitation bandwidth. The average errors were less than the maximum errors mentioned in Secs. III.B–III.D. Errors were small but slightly increased in magnitude and scatter with the amount of feedback. In the limit, the control surfaces attempt to cancel the responses created by other inputs while introducing significant amounts of measurement noise into the command path. The frequency response estimates degrade in this case because of lower signal-to-noise ratios. Regardless of the

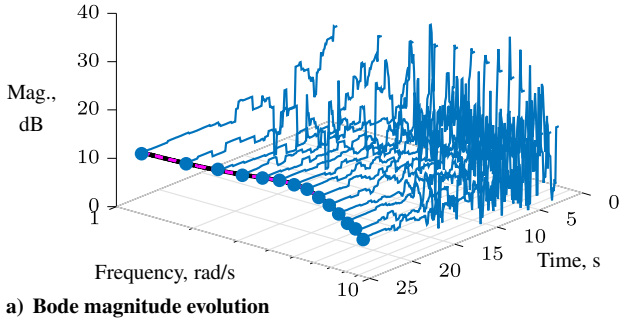

a) Bode magnitude evolution

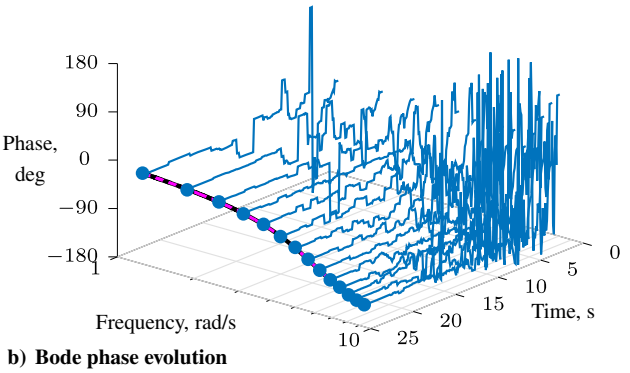

b) Bode phase evolution

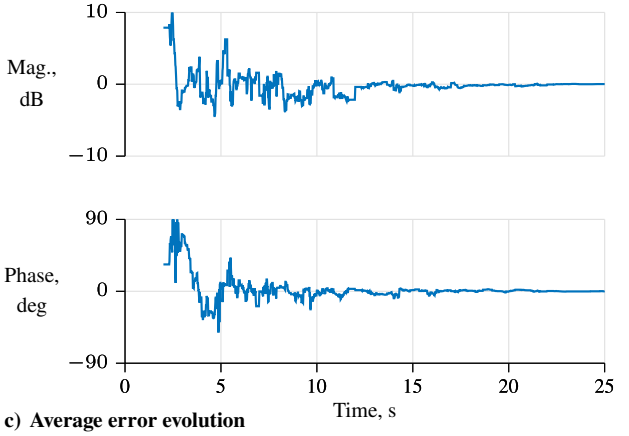

c) Average error evolution

Fig. 9 Real-time estimates of a_z/δ_{eo} for T-2 simulation with multiple-loop closures.

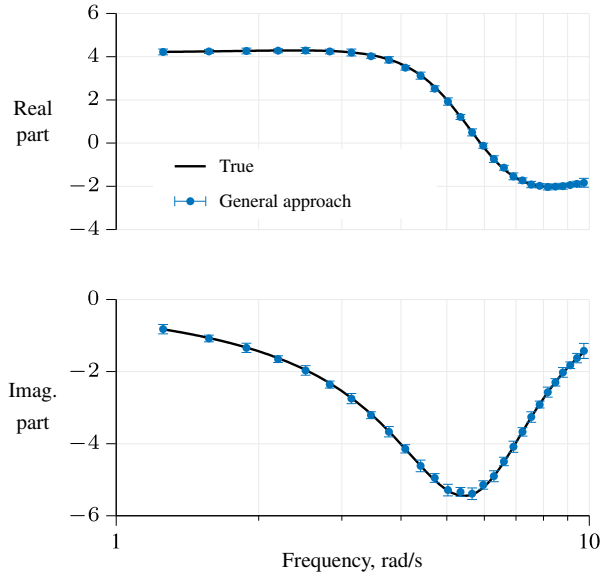

Fig. 10 Effect of measurement noise on a_z/δ_{eo} frequency response estimates. Markers indicate mean and 2σ variation of 500 simulation runs.

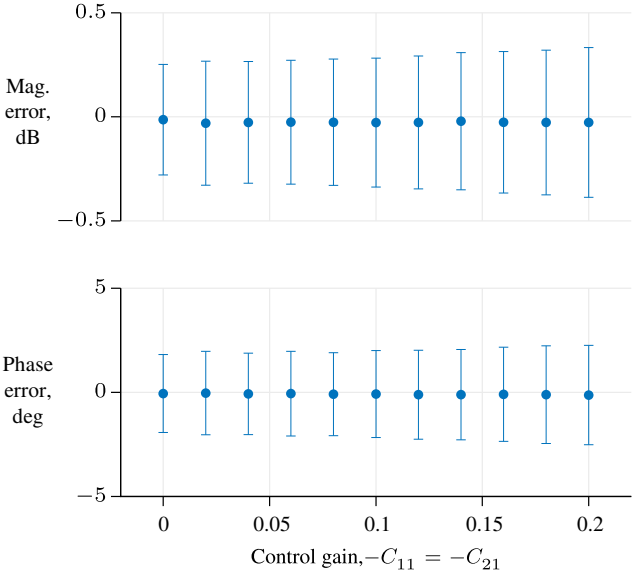

Fig. 11 Effect of augmentation level on average a_z/δ_{eo} frequency response error. Markers indicate mean and 2σ variation of 500 simulation runs.

amount of feedback, the excitations should be designed to create responses with high signal-to-noise ratios but that remain within the linear region.

The effects of bare-airframe damping ratio and multisine harmonic resolution on the accuracy of the general approach were also examined. Details for three cases of damping ratios are listed in Table 5. The first case was the same as in Sec. III.D, whereas in the second and third cases, the stability derivative C_{m_q} was altered to decrease the bare-airframe damping ratio. The control gains C_{11} and C_{21} were selected to achieve approximately the same closed-loop natural frequency as in the baseline case. Designing for the same closed-loop damping ratio would have moved the natural frequencies beyond the bandwidth of excitation. The multisine harmonic frequencies were also progressively thinned by factors of 1, 2, and 3, resulting in 14, 7, and 5 frequencies per input. Each marker in Fig. 12 indicates the average and 2σ variation in the frequency response error for 500 simulation runs. As fewer harmonic frequencies were included, the interpolation accuracy near the modal resonance degraded and the average error increased. In the baseline case, the average error increased from -0.03 ± 0.15 dB to -0.09 ± 0.25 dB in magnitude as the number of harmonic frequencies decreased. This trend was similar but more pronounced for lower bare-airframe damping ratios. Some accuracy can be recovered by using higher-order interpolation to better approximate lightly damped resonances. However, if lightly damped bare-airframe modes are of interest, the multisines should be designed to provide sufficient frequency resolution if feedback or mixing is present. This frequency resolution issue is due to the interpolation and does not affect the analysis of open-loop systems using the basic approach. Good estimates can be achieved for well-damped systems even when frequency resolution is relatively sparse, as shown in the baseline case.

Table 5 Cases for examining bare-airframe damping ratio and frequency resolution on frequency response accuracy

Case	Bare airframe			Closed loop		
	C_{m_q}	ζ	ω_n	C_{11}, C_{21}	ζ	ω_n
1	−37.1	0.43	5.9	−0.10	0.68	7.7
2	+12.7	0.10	5.2	−0.16	0.51	7.7
3	+25.3	0.01	4.9	−0.17	0.47	7.6

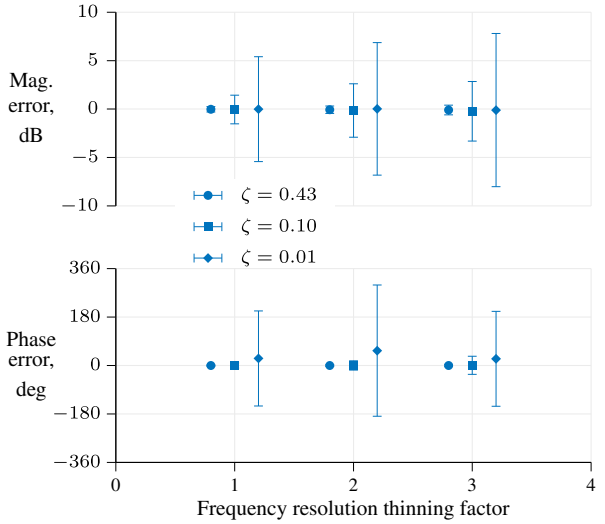

Fig. 12 Effect of frequency resolution and modal damping ratio on average a_z/δ_{eo} frequency response error. Markers indicate mean and 2σ variation of 500 simulation runs.

Fig. 13 X-56A airplane (credit: NASA/Jim Ross).

IV. X-56A Flight Test Results

This section presents results using flight test data from the X-56A Multi-Use Technology Testbed (MUTT) airplane, which is shown in Fig. 13. The aircraft is a subscale aeroelastic demonstrator, designed for studying aeroelastic modeling and control technologies [15]. The maneuver analyzed included multisines on five symmetric control surface pairs, applied after the aircraft was trimmed for straight and level flight at 48% fuel and 63% of the flutter speed. Measured pitch rate and combinations of measured vertical accelerations were fed back to the innermost and outermost control surface pairs δ_{bfs} and δ_{wf4s}. Feedback was also applied to the virtual elevator command, which was sent to the midspan surface pairs δ_{wf2s} and δ_{wf3s} equally. Therefore, both feedback and mixing were present during this maneuver. The remaining midspan pair δ_{wf1s} did not contain feedback or mixing.

Multisine perturbations were summed with other commands from the pilot and flight control system just before the actuator command position limiters. Time histories of the measured control surface deflections for one excitation period are shown in Fig. 14a. The input correlation coefficients were less than 0.3 in absolute value. Also shown is the output time history of a pitch-rate gyroscope located near the nose of the aircraft. No numbers are given on the axes because the flight test data are International Traffic in Arms Regulations (ITAR) restricted. However, these data represented small-amplitude perturbations about the target flight condition.

The Fourier transform magnitudes for the input and output data are shown in Fig. 14b. The multisines had 25 harmonics per input, uniform power, and a bandwidth spanning the short period (SP) and first symmetric wing bending mode (SW1B). Different colors again distinguish the multisine design frequencies, and the plot is annotated with the identified SP and SW1B resonant frequencies. The actuator dynamics created a mild roll-off in amplitude with frequency, and the feedback and mixing were evident in the additional frequency content of the signals. The measured pitch rate contained content from all harmonic frequencies, particularly those from the outboard control surfaces due to the larger moment arms.

Estimated frequency responses from the three outermost surfaces to the measured pitch rate are shown in Fig. 15. The same magnitude, phase, and frequency scales were used for each Bode plot. The amplitudes of the δ_{bfs} and δ_{wf1s} surfaces were too small to compute accurate frequency responses, as seen by the small magnitudes in the pitch-rate data in Fig. 14b. The basic and general approaches had different results for each Bode plot, particularly for $q^{\text{gyr}}/\delta_{wf4s}$.

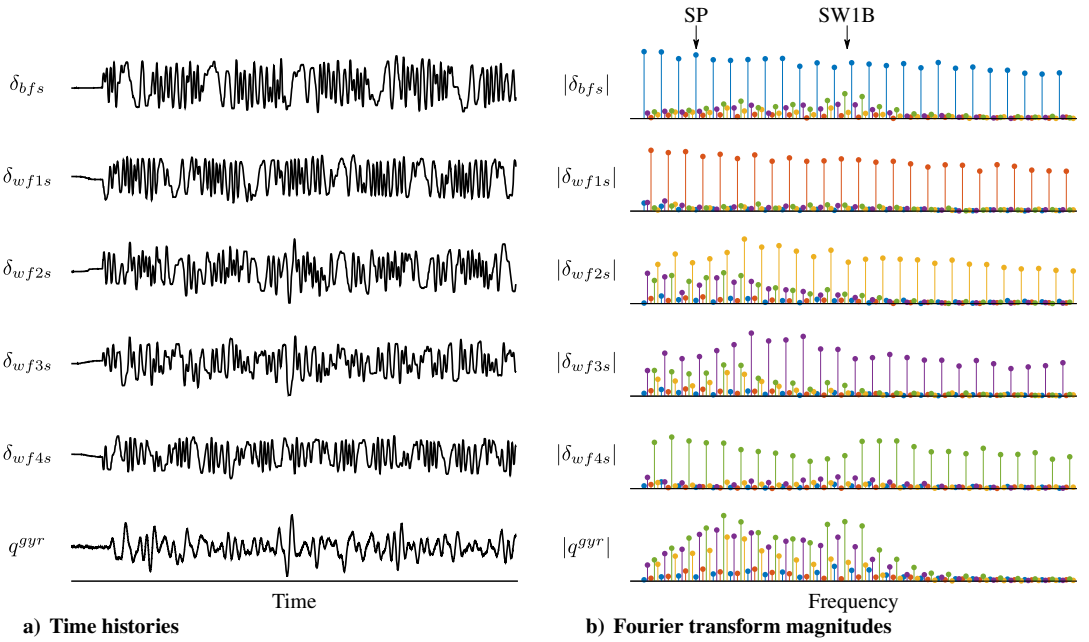

a) Time histories **b) Fourier transform magnitudes**

Fig. 14 X-56A flight test data with feedback and mixing.

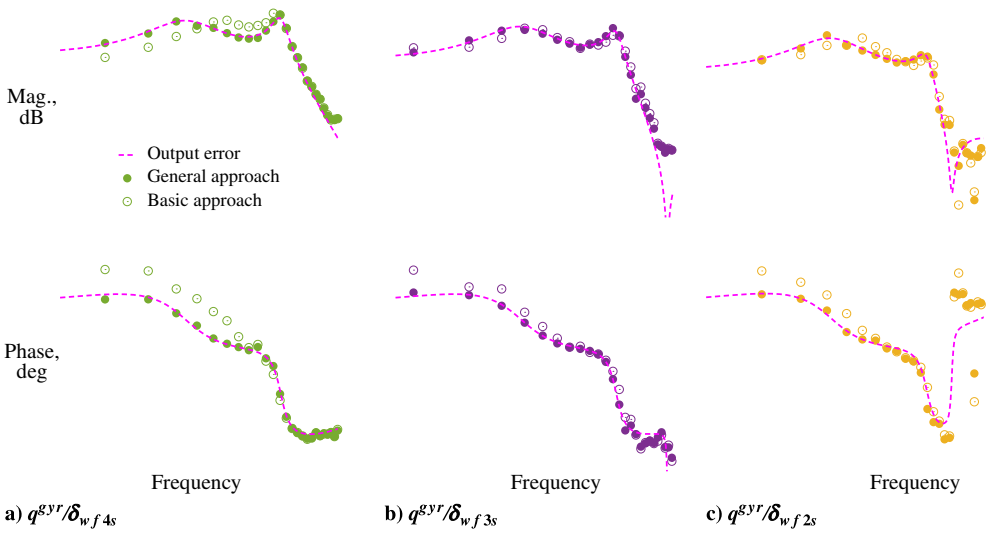

Fig. 15 Frequency response estimates for X-56A flight test data with feedback and mixing.

These differences occur near the SP and SW1B modes, which is within the control system bandwidth. The frequency responses estimated with the basic approach incorrectly produced a higher short-period frequency, lower SW1B frequency, and a phase angle offset in the frequency range up to the SW1B mode.

The dashed purple lines are the frequency responses of a state-space model identified using output error to match Fourier transforms of gyroscope and vertical accelerometer data (not shown). In addition to estimating nondimensional stability and control derivatives for the aeroelastic model, time delays for each of the outputs were also estimated. More information about these results can be found in Ref. [16]. The frequency responses obtained using output error agreed with the frequency responses computed using the general method, indicating that frequency resolution was not an issue and corroborating the results of the general approach for frequency response estimation.

V. Conclusions

A method was developed for computing MIMO frequency response estimates of dynamic systems when the inputs include excitations from orthogonal phase-optimized multisines and when feedback control or mixing is present. A previous approach based on output and input Fourier transform data was extended using interpolation to resolve the confounding effects from feedback and mixing. The method was developed in simulation and verified using flight test data. Advantages and limitations of the approach were discussed.

The proposed method can produce accurate results when modeling assumptions are adhered to during the experiment. The presented results using the general approach closely matched those computed from other models identified using the maximum likelihood output-error approach, which is less sensitive to correlation issues. The cost of the approach is injecting computerized excitations and flying in calm air. The benefits include the straightforward computation of frequency responses using multiple inputs and multiple outputs from a single flight test and in real time.

Acknowledgments

This research was supported by the NASA Advanced Air Transport Technology (AATT) Project. The efforts of the X-56A team at NASA Armstrong Flight Research Center (AFRC) are gratefully acknowledged. Discussions with the X-56A team members and Eugene Morelli are appreciated.

References

[1] Morelli, E., and Klein, V., *Aircraft System Identification: Theory and Practice*, 2nd ed., Sunflyte, Williamsburg, VA, 2016, pp. 115–508.

[2] Klein, V., and Murphy, P., "Aerodynamic Parameters of High Performance Aircraft Estimated from Wind Tunnel and Flight Test Data," NATO RTO-MP-11, 1998.

[3] Tischler, M., and Remple, R., *Aircraft and Rotorcraft System Identification: Engineering Methods with Flight Test Examples*, 2nd ed., AIAA, Reston, VA, 2012, pp. 163–328. doi:10.2514/4.868207

[4] Ljung, L., *System Identification: Theory for the User*, 2nd ed., Prentice Hall, Upper Saddle River, NJ, 1999, pp. 173–178, 428–440. doi:10.1109/MRA.2012.2192817

[5] Knapp, M., Berger, T., Tischler, M., Cotting, M., and Marcus, A., "Development of a Full Flight Envelope F-16 VISTA Simulation Model from Closed-Loop Flight Data," AIAA Paper 2018-0525, 2018. doi:10.2514/6.2018-0525

[6] Berger, T., Tischler, M., Knapp, M., and Lopez, M., "Identification of Multi-Input Systems in the Presence of Highly Correlated Inputs," *Journal of Guidance, Control, and Dynamics*, Vol. 41, No. 10, 2018, pp. 2247–2257. doi:10.2514/1.G003530

[7] Grauer, J., and Morelli, E., "Method for Real-Time Frequency Response and Uncertainty Estimation," *Journal of Guidance, Control, and Dynamics*, Vol. 37, No. 1, 2014, pp. 336–344. doi:10.2514/1.60795

[8] Grauer, J., "Aircraft Fault Detection Using Real-Time Frequency Response Estimation," AIAA Paper 2016-0372, 2016. doi:10.2514/6.2016-0372

[9] Grauer, J., "Dynamic Modeling Using Output-Error Parameter Estimation Based on Frequency Responses Estimated with Multisine Inputs," NASA TM-2018-220108, Nov. 2018.

[10] Morelli, E., "System IDentification Programs for AirCraft (SIDPAC)," Version 4.1, NASA Software Catalog, http://software.nasa.gov [retrieved Dec. 2018].

[11] Morelli, E., "Multiple Input Design for Real-Time Parameter Estimation in the Frequency Domain," International Federation of Automatic Control Paper REG-360, 2003. doi:10.1016/S1474-6670(17)34833-4

[12] Morelli, E., "Flight-Test Experiment Design for Characterizing Stability and Control of Hypersonic Vehicles," *Journal of Guidance, Control, and Dynamics*, Vol. 32, No. 3, 2009, pp. 949–959. doi:10.2514/1.37092

[13] Milliken, W., "Progress in Dynamic Stability and Control Research," *Journal of the Aeronautical Sciences*, Vol. 14, No. 9, 1947, pp. 493–519. doi:10.2514/8.1434

[14] Pintelon, R., and Schoukens, J., *System Identification: A Frequency Domain Approach*, 2nd ed., Wiley, Hoboken, NJ, 2012, pp. 33–72. doi:10.1002/9781118287422

[15] Beranek, J., Nicolai, L., Buonanno, M., Atkinson, C., Holm-Hansen, B., and Flick, P., "Conceptual Design of a Multi-utility Aeroelastic Demonstrator," AIAA Paper 2010-9350, 2010. doi:10.2514/6.2010-9350

[16] Grauer, J., and Boucher, M., "Identification of Aeroelastic Models for the X-56A Longitudinal Dynamics Using Multisine Inputs and Output Error in the Frequency Domain," *Aerospace*, Vol. 5, No. 2, 2019, pp. 1–25. doi:10.3390/aerospace6020024

This article has been cited by:

1. Eugene A. Morelli. Practical Aspects of Multiple-Input Design for Aircraft System Identification Flight Tests . [Abstract] [PDF] [PDF Plus]
2. Jared A. Grauer. An Interactive MATLAB Program for Fitting Transfer Functions to Frequency Responses . [Abstract] [PDF] [PDF Plus]
3. Jared A. Grauer, Matthew J. Boucher. 2020. Aircraft System Identification from Multisine Inputs and Frequency Responses. *Journal of Guidance, Control, and Dynamics* **43**:12, 2391-2398. [Citation] [Full Text] [PDF] [PDF Plus]
4. Jared A. Grauer, Matthew Boucher. System Identification of Flexible Aircraft: Lessons Learned from the X-56A Phase 1 Flight Tests . [Abstract] [PDF] [PDF Plus]
5. Jared A. Grauer, Matthew Boucher. Aircraft System Identification from Multisine Inputs and Frequency Responses . [Abstract] [PDF] [PDF Plus]